Award Number: G09AP00054

EARTHQUAKE SOURCE AND GROUND MOTION CHARACTERISTICS IN THE CENTRAL AND EASTERN UNITED STATES

Final Report

October 29, 2010

Paul Somerville and Sidao Ni
(Contact Email: Paul_Somerville@URSCorp.com)

URS Group, Inc.
566 El Dorado Street
Pasadena, CA 91101-2560
Tel: (626) 449-7650
Fax: (626) 449-3536

Abstract

Our goal is to develop improved high frequency earthquake source and wave propagation models for the Central and Eastern United States (CEUS) for subsequent use in enhancing our ground motion prediction model for the CEUS. The data base of strong motion recordings in the Central and Eastern United States is too sparse to permit the development of empirical ground motion prediction models based purely on recorded data, necessitating the use of seismologically based methods. We first collect broadband ground motion recordings of ENA M>4.5 earthquakes, and then obtain robust source parameters such as a seismic moment, focal mechanism solution and focal depth for each event that is insensitive to the crustal structure using very long period waves. With the precise source parameters fixed, we refine velocity models in CEUS with forward waveform modeling, surface wave dispersion as well as waveform inversion. Waveform inversion is based on differential Green's function of layered crustal structure and conjugated gradient method. Moho depth is found to vary from the central US to the eastern US, and the top 1km of CEUS structure shows much higher shear velocity (~2.9km/s). Using these refined earthquake source and crustal structure models developed for each event, we generate broadband ground motion simulations (0.1-10Hz) with an improved frequency-wave number algorithm. This new algorithm features a deterministic radiation pattern at low frequency and a gradually more stochastic radiation pattern for frequencies above the transition frequency. The CEUS events are found to have higher transition frequency (1.5-2Hz) than those in the western US (1Hz). Both synthetic and observed seismograms show frequency dependent radiation patterns. We determine a whole path Q model for the crust, and find that Q is much higher in the CEUS than that in the western US. High frequency (2Hz-50Hz) ground motion simulations are computed with a ray code that accounts for layered crustal structure, frequency dependent Q, direct rays and Moho-reflected rays, as well as a stochastic finite fault distribution of sub-fault sources. Synthetic high frequency ground motion simulation with only S waves agrees well with observations, but observed P waves also produce non-negligible high frequency ground motions which require more studies in the future. We conclude that it is indeed feasible to simulate broadband ground motion in the CEUS with reliable source parameters from long period waveform inversion, refined velocity models from improved source parameters and improved Q models from well resolved source parameters and velocity models.

1. Earthquake Source Parameters from Waveform Modeling

We collected broadband waveform data for M4.5+ events as well as some shallow events in CEUS (table 1). These events are recorded by IRIS GSN stations, New Madrid Cooperative Seismic network (NM), Lamont-Doherty Cooperative Seismographic Network (LCSN) and United Stations National Seismic Network (USNSN). All the broadband seismograph stations have three components, and typically have sampling rate of 20 points per second, therefore providing maximum frequency coverage up to 10Hz. But for some recent stations, the sampling rate is 100

point per second, thus allowing ground motion studies up to 50Hz. Instrument responses of these seismograph stations are well calibrated, and are removed before any waveform modeling is performed. Horizontal components are rotated into radial and tangential components so that long period waveform modeling can be conveniently performed.

Table 1. Earthquakes with broadband waveforms modeled in this project

Date	Location	Lat(North)	Long(West)	Depth	Mag	Mechanism
2008/04/18	Mt Carmel, Illinois	38.45	87.89	15	Mw5.2	strike-slip
2002/06/18	Caborn, Indiana	37.99	87.77	18	Mw4.5	Strike-slip
2002/04/20	Au Sable Forks	44.51	73.70	11	Mw5.0	reverse
2009/02/03	Rockaway, New Jersy	40.87	74.52	2-5	Mc3	N/A

There are three events with magnitude greater than M4.5 in the CEUS Since 2000. Among them, the April, 18, 2008 Mt Carmel, Illinois earthquake is the strongest and the best recorded event (Figure 1). Both long period (>5s) and high frequency signals from this event (>2Hz) show high signal to noise ratio for distances up to 500km. All the three events have been modeled by Herrmann et al., 2008. The 2002 Caborn earthquake and the 2002 Au Sable earthquake were also studied by Seeber et al (2002) and Kim (2003). They inverted the source parameters (moment, focal mechanism and focal depth) with a full waveform approach, in which the misfit function is computed between the whole waveforms of recorded and synthetic seismograms.

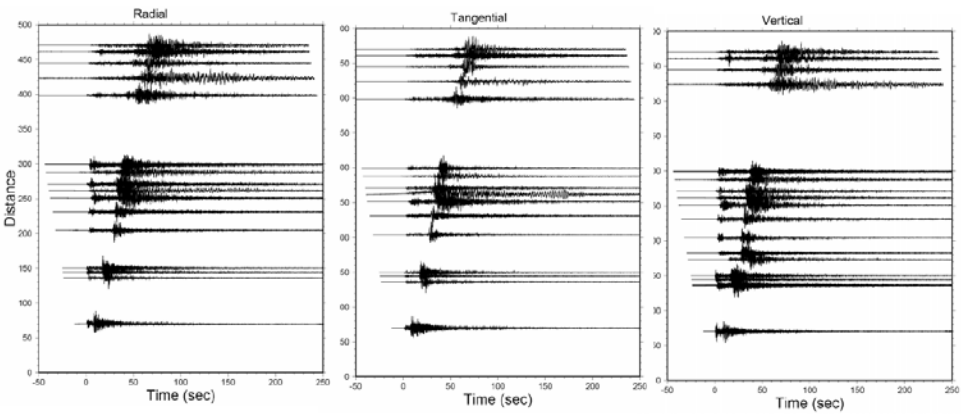

Figure 1. Three component broadband record sections of the 04/18/2008 Mt Carmel earthquake. Radial, tangential and vertical components are displayed on the left panel, middle panel and right panel respectively.

We verified or refined the source parameters of these earthquakes with a different algorithm. The source inversion is performed with the Cut and Paste method (CAP) (Zhu and Helmberger, 1996). In this algorithm, full waveforms are cut into the Pnl segment and the S+surface segment. Each segment is fit with synthetic seismograms separately. The CAP algorithm is basically a grid search inversion with synthetic seismograms calculated for a 1D layered crustal model appropriate for the area, with time shifting of the Pnl and

surface wave parts to allow for inaccuracy in the velocity model (Zhu and Helmberger, 1996). Moreover, the amplitude of the waveforms is also adjusted according to their distances in order to suppress overweighting of close stations, thus leading to a much more balanced inversion of the source mechanism. Focal depth can also be well resolved because the Pnl waveform is sensitive to focal depth and the amplitude ratio between the surface wave and the Pnl wave provides good constraints on focal depth.

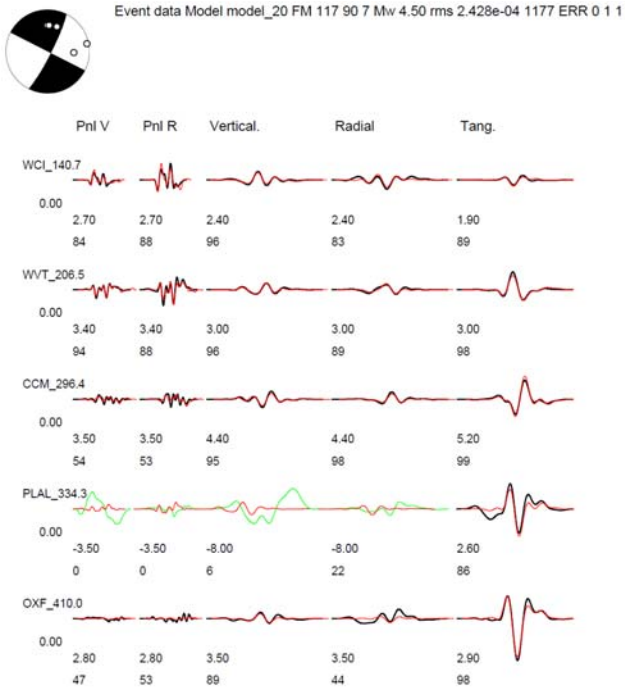

Figure 2. "Cut and Paste" (CAP) modeling of the Pnl and Surface waves for the 06/18/2002 Caborn event. Pnl waves are filtered with bandpass 0.02-0.3Hz and the surface waves are filtered at 0.01-0.2Hz. The event occurred at a depth of 19km, with an almost pure strike-slip mechanism. The distances in km are noted after the station names along with the P-timing correction. The numbers beneath the various waveform segments indicate the timing shifts and cross-correlations. There are some anomalies on the PLAL waveforms (green), which are not used in the inversion.

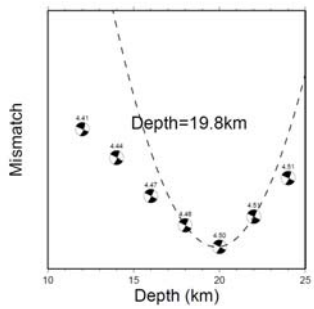

Figure 3. Depth sensitivity from CAP inversion of the Caborn event. The optimal estimate of depth is 19.8km, close to that obtained by Kim (2003).

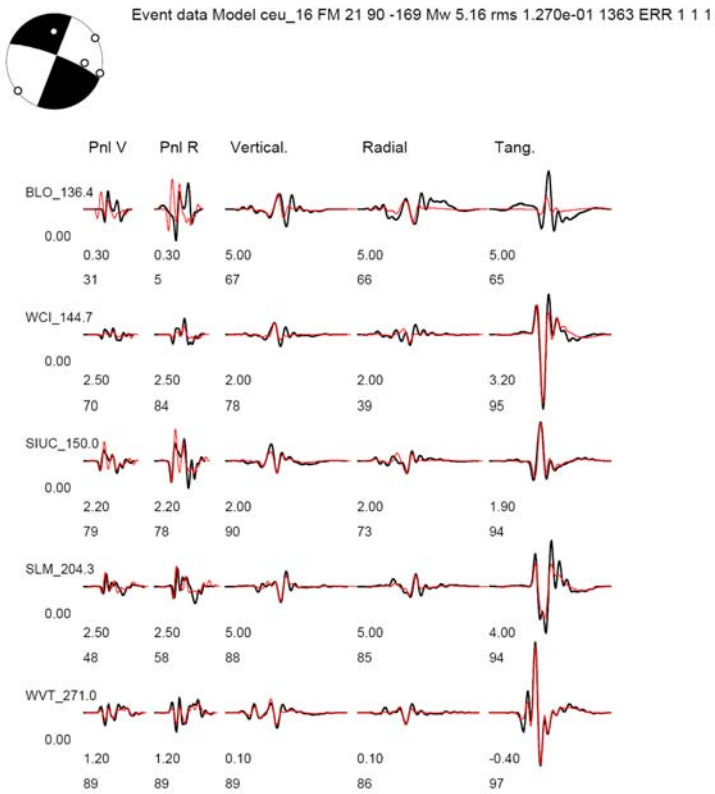

Figure 4, "Cut and Paste" (CAP) modeling of the Pnl and Surface waves for the Mt. Carmel event. Because of its larger moment, the signal noise ratio is much higher than that of the Caborn event.

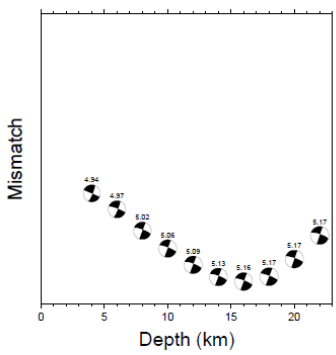

Figure 5. Depth sensitivity from CAP inversion of the Mt Carmel event. The optimal estimate of depth is 16 km, close to that obtained by Herrmann et al (2008).

We performed CAP inversion for the 06/18/2002 Caborn, Indiana earthquake and the 04/18/2008 Mt Carmel, Illinois earthquake (Figures 2 through 5). Both events show dominant strike slip mechanism, which may reflect the same regional stress. But their focal depths are different, with the Carborn event at a depth of 19.8km and the Mt Carmel at a depth of 16.0km. Focal mechanisms from CAP inversion are consistent with those from whole waveform inversion (Herrmann et al., 2008; Seeber et al., 2002; Kim, 2003). But the focal depths from CAP inversion are different from those from whole waveform inversion by 1-2km. Such difference in depth solution is not surprising, because the focal depth solution can be affected by factors such as

different 1D velocity models, or 3D heterogeneity and different inversion schemes. For example, focal depth solutions from two agencies (Lamont Observatory and Saint Luis University) for the 2002 Au Sable earthquake are 10 km and 11km respectively. However Ma and Atkinson (2006) find that the focal depth is 12km from analysis of the depth phase sPn. To assess the accuracy of the depth solution resolved from local or regional waveforms, we computed synthetic teleseismic P waves for the case of focal depth=10km (Figure 6). It seems that a focal depth of 10km can fit the observed P waves (red) fairly well and the different focal mechanisms also provide good waveform fits.

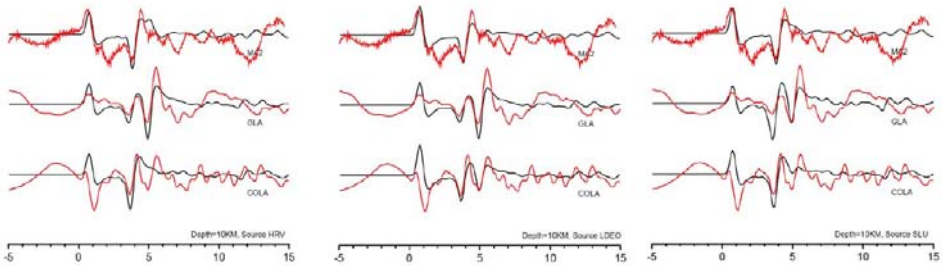

Figure 6. Comparison of observed (red) and synthetic teleseismic P waveforms with source parameters from different agencies (Left, Harvard CMT; Middle, Lamont Observatory; Right, Saint Luis University). The Lamont solution provides a slightly better waveform fit.

After we perform CAP inversion for the events, we find that seismic moments from our inversion typically differ less than 0.05 magnitude unit from solutions by other groups (Herrmann et al, 2008; Kim, 2003), and fault planes solutions are different within 5 degrees (strike, dip and rake). Focal depths are different by at most 2km. However, the Harvard CMT typically provides depth solutions up to 5km different from our solution.

2.Velocity Structure from forward waveform modeling and inversion

2.1 Velocity Structure of the Shallow Crust from Surface Wave Dispersion

Typically the top 1km of the velocity structure of the Crust is not well resolved by seismologists for the purpose of earthquake studies, probably due to the fact that 1km is too deep for earthquake engineering studies and too shallow to be imaged by seismic waves from most natural earthquakes. However, for regions with very shallow earthquakes (depth less than 2km), the strong short period surface waves (such as Rg) may provide good constraints on shallow velocity structure. On February 3rd, 2009, an Mc3 earthquake occurred in New Jersey and was well recorded by nearby seismograph stations with epicentral distance less than 30km (Figure 7). It is clearly a shallow event because the short period Rg (dominant period about 1 sec) is very strong, and probably it is shallower than 1km (Figure 8, left). We measured the dispersion curve of Rg on station BRNJ, and found that the Rg group velocity

increases substantially with depth (Figure 8, right). Because Rg dispersion is observed for the period range between 0.4s and 2 second, the velocity structure for a depth of about 2km can be obtained. The shear velocity profile inverted from Rg dispersion is displayed in Figure 9, which features large sub-surface shear velocity (Vs~2.9 km/s) and shear velocity increasing to 3.6 km/s (usually indicative of crystalline basement) at a depth of 1.5km. This is in obvious contrast to the shallow shear velocity structure in the western US, where a shear velocity of 3.3 km/s is achieved at a depth of about 4 km, and the subsurface Vs is much lower The large subsurface Vs of 2.9 km/s in Figure 9 is consistent with Herrmann's model (Herrmann et al., 2008), and is probably related to the old and cold shallow crust of CEUS, which also implies high Q and less attenuation of high frequency ground motion at large distances.

Figure 7. A shallow earthquake occurred on February 3rd, 2009 in New Jersey. This event is well recorded by nearby broadband stations (ODNJ, BRNJ, MSNJ).

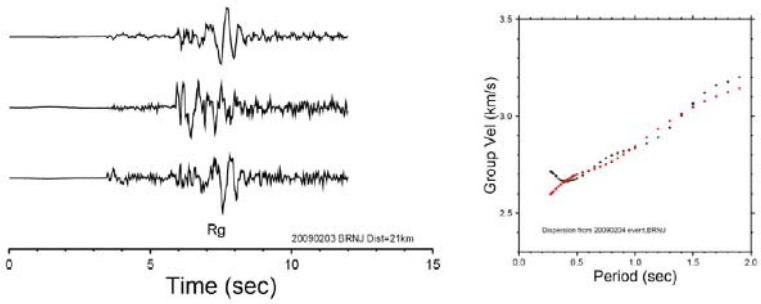

Figure 8. (left) Three component broadband seismic waveforms recorded at station BRNJ. The shallow focal depth is manifested by the strong Rg wave. (right) Measured Rg dispersion (black) and synthetic dispersion for the model displayed in Figure 9.

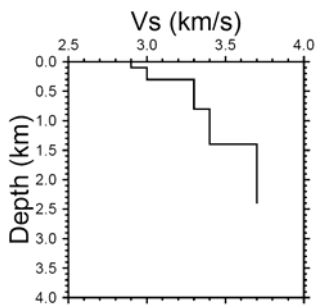

Figure 9. Velocity model for computing synthetic dispersion. Because Rg is a short period surface wave, only the velocity structure of the shallow crust can be well constrained from Rg dispersion.

2.2 Velocity Structure of the Deeper Crust

To determine the velocity structure of the deep crust, we adopted the waveform inversion approach by Saikia et al (2006). This method determines the first-order velocity perturbations (Δm) of the initial velocity model by inverting the data vector (Δd) formed using the difference between the observed and synthetic seismograms. Thus, it is essentially a least-squares inversion, and its formalism can be expressed as

$$\Delta d = DG\,\Delta m$$

where DG is the first-order partial derivative and represents the differential change in the seismogram for a differential change in a single-model parameter. Assuming that CEUS crust can be approximated with 1D models, the crustal model m is parameterized as vectors of P velocity, S velocity and Density. Because seismograms are not sensitive to density, we scale density with P velocity (Magistrale et al., 2000). Differential seismograms are computed by differencing synthetic seismograms for model m and perturbed velocity model ($m+\Delta m$). As compared to the algorithm developed by Zeng and Anderson (1995), our approach to computing differential seismogram is less efficient because N times the number of synthetic seismograms need to be computed, where N is the number of layers in model m while Zeng and Anderson's algorithm can provide differential seismograms in one run. But our approach is easy to implement and the computing cost is not a big issue for 1D synthetic seismograms.

Before waveform inversion for crustal structures, source parameters such as fault plane solution, depths and seismic moment of the earthquakes need to be resolved (Section 1). In Figure 10, we display a comparison of observed seismograms and synthetic seismograms for an initial model for an earthquake recorded at station CCM. Obviously, the initial model does not provide a good waveform fit to the S wave (around 40 seconds). After inversion, the waveform fit is much better. Waveform inversion for velocity structure is highly nonlinear, and good initial velocity models are necessary to obtain stable and converging inversions. The initial velocity model is taken from Saikia et al. (2006) (Figure 11).

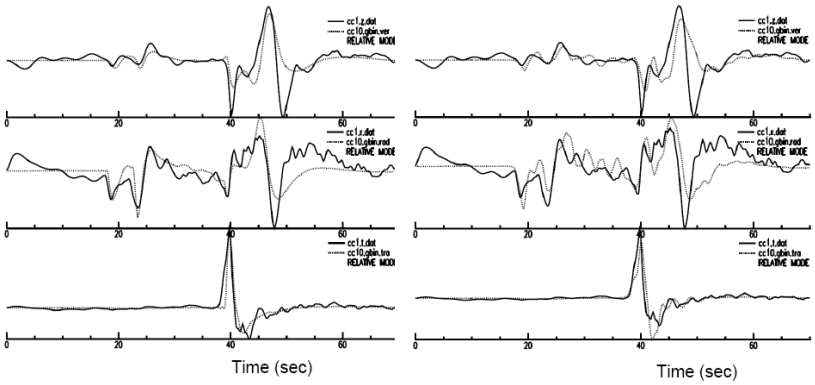

Figure 10. Comparison of observed seismograms (solid line) and synthetic seismograms (dashed) for initial model (left) and final model (right). The seismograph station is CCM.

For different station-earthquake pairs, many 1D velocity models can be obtained. We find that most of the 1D models are very close to the velocity model by Herrmann

et al. (2008). So we choose Herrmann's model as the representative model for CEUS. From forward waveform modeling, we find that the model works very well for the central US, but fine tuning is necessary for fitting seismograms for earthquake- station pairs in the eastern US. In Figure 11 (right), we can observe that synthetic (red) seismograms computed with Herrmann's model (Moho depth=42km) do not match the observations (black) well for the Au Sable earthquake recorded at station HRV. We then try a suite of models with different Moho depths, and find that a Moho depth of 36km (orange line in middle panel of Figure 11; model 9) can produce a much better waveform match for both station HRV and NCB (Figure 12). Of course, there is a drawback with forward modeling in that different models can fit the observations equally well (left panel and middle of Figure 12, model 9 and model 5, the blue model indicated with blue line in Figure 11), but these models are fairly similar.

In short, 1D models for central US and eastern US are different, and difference in Moho depth is probably the major distinction.

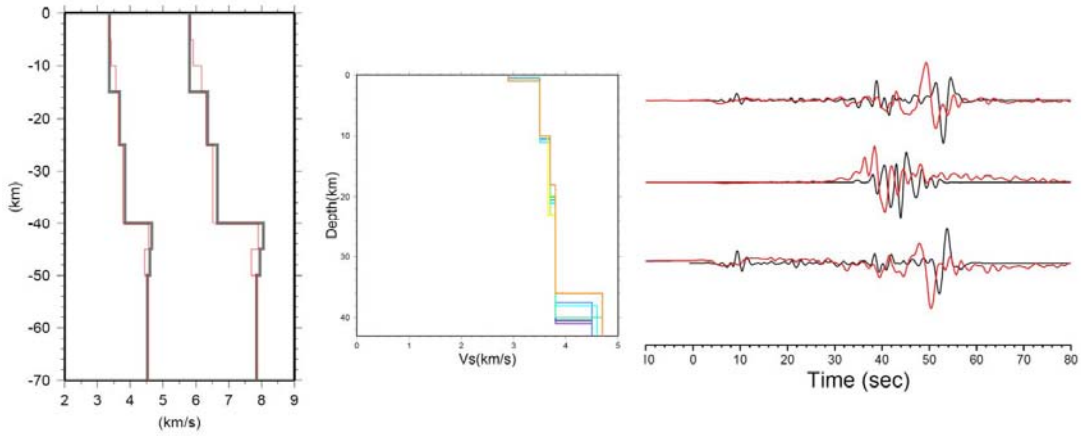

Figure 11. (left) initial model (black) and final model from waveform inversion (middle) various models modified from Herrmann's model. (right) Observed (black) and synthetic (red) seismograms with Herrmann's model for the Au Sable earthquake recorded at station HRV.

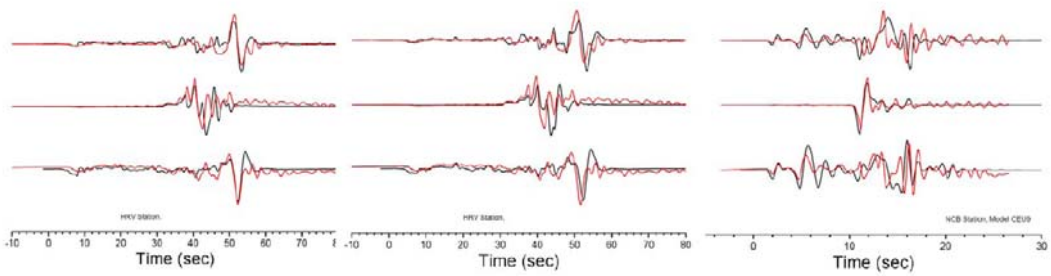

Figure 12. Observed (black) and synthetic (red) seismograms calculated using the velocity models shown in Figure 11. (left) model 5 at station HRV (center) model 9 at station HRV (right) model 9 at station NCB.

3. Modeling transition frequency between deterministic and stochastic character

3.1 Observation of frequency dependent radiation effects

We observe a decrease in the coherence of the radiation pattern with increasing frequency in strong ground motions, which is presumably due to irregularities in fault geometry and scattering effects. For the Mt Carmel earthquake (Figure 13), the tangential (red) component should be much stronger than the radial (green) and vertical (black) component because the source mechanism is dominantly strike-slip (Figure 14). Indeed this is the case for low frequencies (<1HZ), but for frequencies above 3Hz, the three components are almost equal. For the Au Sable earthquake, similar features are observed, where the ratio between tangential and radial or vertical are different for low frequencies and high frequencies. The transition frequency is between 1Hz and 3Hz, and is probably at about 2Hz.

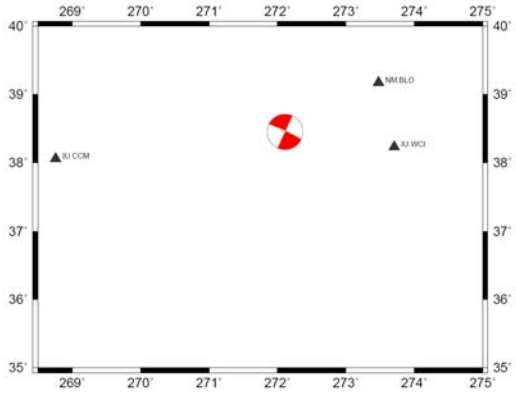

Figure 13. The Mt Carmel earthquake and three broadband stations

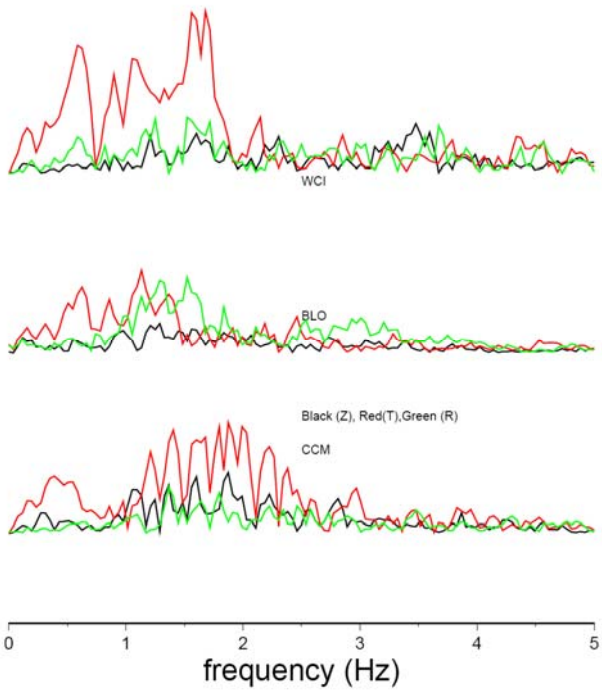

Figure 14. Spectrum of observed ground velocity for the three stations.

For both events, the three components become almost equal at high frequencies (Figure 15), indicating that seismic radiation is isotropic at high frequencies. Therefore, the radiation pattern of earthquakes in the CEUS is indeed frequency dependent. The 2Hz transition frequency is higher than the transition frequency of 1Hz for western US (Graves and Pitarka, 1999), implying less heterogeneity in CEUS which is probably due to less tectonic activity in this region.

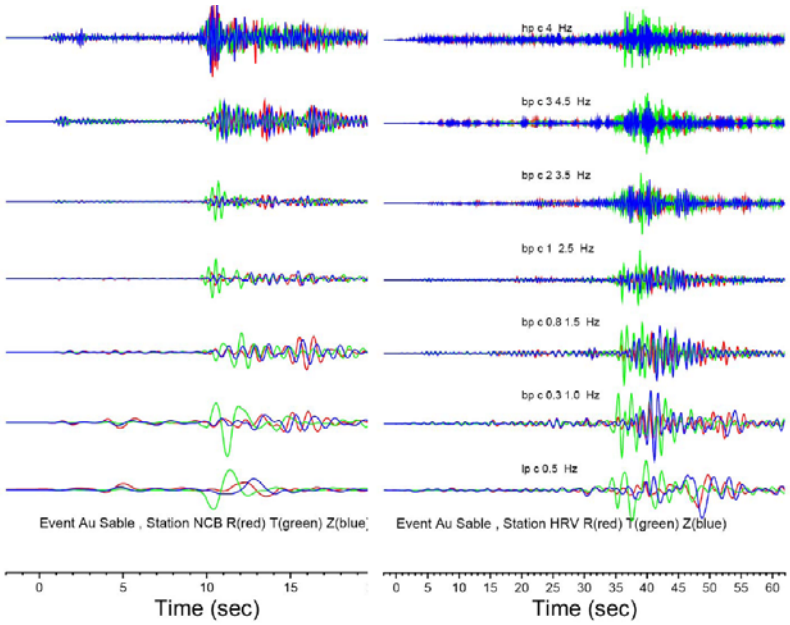

Figure 15. Decrease of coherence of radiation pattern at high frequency for the Au Sable event observed at station NCB (left) and HRV (right). The top and bottom traces are filtered with high pass and low pass filters respectively, while the other traces are filtered with band pass filters.

With weak tectonic deformation, the crustal structure in the Central and Eastern US (CEUS) is relatively simple and justifies a 1D layered model parameterization. For overall 1D crustal structure, the hybrid method of ground motion simulation can be approached within a 1D framework. The hybrid method consists of deterministic waveform simulation for low frequency (1HZ) with complete Green's function (from F-K method, i.e., solution in frequency-wave number domain) and stochastic modeling for high frequencies also with the F-K method. Stochastic modeling is required because of imperfect knowledge of rupture processes and small scale 3D velocity structure along the propagation path. For the source portion of stochastic modeling, interpolation of radiation effects for the transition from deterministic to stochastic modeling can be readily implemented in an F-K algorithm since F-K works in the frequency domain. For the 3D structure portion of stochastic modeling, cross-component scattering has to be introduced to transfer energy from different components. The scattering effect is also parameterized as a function of the ratio of epicentral distance to wavelength, which also features transition from deterministic (no scattering for low frequency,) to stochastic (energy equalization for high frequency). Interpolation of scattering effects is also implemented in the frequency domain.

3.2 An algorithm for computing broadband ground motion in a unified framework

The idea of deterministic low frequency and stochastic high frequency modeling has proven effective in simulating ground motion. Techniques for low frequency waveform modeling include 3D finite difference (Graves, 1999; Pitarka, 1998;), 3D spectral element method (Komatitsch and Tromp, 1999) and 1D frequency wave number methods (Zhu and Rivera, 2002). Stochastic high frequency algorithms have been applied by various researchers with different approaches, such as empirical geometric spreading (Atkinson, 2004), computed geometric spreading (Ou and Herrmann, 1994; Graves and Pitarka, 1999), generalized ray theory (Somerville et al, 1999) and frequency-wave number (FK) algorithm (Liu et al, 2006).

In this project, we simulate ground motion in a single F-K algorithm for both deterministic and stochastic frequency ranges. The attenuation (absorption, Q) is already taken into account in the FK algorithm, with Q specified for each layer. For double couple sources in 1D models, the ground motion (in velocity, acceleration or displacement) can be calculated if Greens' functions for 3 basic faulting mechanism (strike-slip, dip-slip and 45 degree dip-slip) are known. Various algorithms have been proposed for calculating Green's functions in a 1D layered model, including generalized ray theory (Helmberger, 1983), and the frequency-wave number method (Saikia, 1994; Zhu and Rivera, 2002). The 3-components of ground motion, vertical (w_z), radial (q_r) and tangential (v_θ) are actually just linear combinations of the vertical (W_i), radial (Q_i) and tangential (V_i) component of the Green's function of 3 basic mechanisms (equation 2-1 to 2-3). The coefficients A_i , also known as radiation pattern, depend on the geometry of the fault (strike Φ, and dip δ) as well as orientation of fault motion (rake λ), and are shown in equation 2-4 to 2-8.

$$w_z(t,r,z,\theta) = S(t) * \sum_{i=1}^{3} A_i(\phi,\delta,\lambda) W_i(t) \qquad (1\text{-}1)$$

$$q_r(t,r,z,\theta) = S(t) * \sum_{i=0}^{3} A_i(\phi,\delta,\lambda) Q_i(t) \qquad (1\text{-}2)$$

$$v_\theta(t,r,z,\theta) = S(t) * \sum_{i=1}^{2} A_{i+3}(\phi,\delta,\lambda) V_i(t) \qquad (1\text{-}3)$$

$$A_1(\phi,\delta,\lambda) = \sin 2\phi \sin\delta \cos\lambda + 0.5\cos 2\phi \sin 2\delta \sin\lambda \qquad (1\text{-}4)$$

$$A_2(\phi,\delta,\lambda) = -\sin\phi \sin 2\delta \cos\lambda + \cos\phi \cos\delta \cos\lambda \qquad (1\text{-}5)$$

$$A_3(\phi,\delta,\lambda) = 0.5\sin 2\delta \sin\lambda \qquad (1\text{-}6)$$

$$A_4(\phi,\delta,\lambda) = \cos 2\phi \sin\delta \cos\lambda - 0.5\sin 2\phi \sin 2\delta \sin\lambda \qquad (1\text{-}7)$$

$$A_5(\phi,\delta,\lambda) = -\cos\phi \cos 2\delta \sin\lambda - \sin\phi \cos\delta \cos\lambda \qquad (1\text{-}8)$$

Earthquake sources can be approximated as patches of slip over a fault plane. At low frequencies, the slip distribution can be reliably inferred from seismic and geodetic data. However at high frequencies the slip distribution (also at higher spatial resolution) is more complicated, and the fault plane is not necessarily smooth at short wavelength. Therefore, at high frequencies, the faulting parameters (Φ,δ,λ) needs to be treated as stochastic, reflecting our insufficient knowledge of the true faulting processes.

To write the above equations in the frequency domain, we have

$$U_j(\omega) = \sum_{k=1}^{k=3} G_{jk}(\omega)\, R_{jk}(\emptyset(\frac{\omega L}{\beta}), \delta(\frac{\omega L}{\beta}), \lambda(\frac{\omega L}{\beta}))$$

where G_{jk} is the *j*th component Green's function for *k*th basic faulting mechanism, and R*jk* is just the coefficient A , with *j*=1 (vertical) ,2 (radial) and 3 (tangential) and *k*=1 (strike slip),2 (45 degree dip-slip) and 3 (90 degree dip-slip). In hybrid the simulation method, R_{jk} is assumed to be deterministic and to not depend on frequency ω for low frequencies. But at higher frequencies, R_{jk} is required to depend on frequency ω to simulate the effects of complex slip distribution upon radiation pattern. Pitarka et al (2000) and Liu et al (2006) proposed linear interpolation of source parameters (Φ, δ, λ) vs frequency. In our approach, we assume that the stochastic portion R_{jk} depends upon the ratio between wave length (shear wave speed β / frequency ω) and rupture dimension (L) This implies a higher transition frequency for smaller earthquakes (Frankel , 2009). Following the approach taken by Pitarka et al (2000), we set the source parameters (Φ,δ,λ) to depend on frequency in the following equation:

$$\varphi = \begin{cases} \varphi_0 & x < x0 \\ \varphi_0 + \dfrac{r_i\, \varphi_p (x - x0)}{x1 - x0} & x0 < x < x1 \\ \varphi_0 + r_i\, \varphi_p & x1 < x \end{cases}$$
$$x = \omega\, L\, /\beta$$

where φ is one of the source parameters (Φ,δ,λ), φ_p is the range of source complexities, r_i is a random number between 0 and 1, and x is the ratio of fault dimension and shear wave length ($\omega L/\beta$) . The ratio x_0, x_1 is chosen to be 1.6π and 4.8 π respectively, approximately corresponding to 1 and 3 Hz for an M5 earthquake (assuming rupture dimension of 3km) in the CEUS.

Though introduction of a stochastic distribution of source parameters can account for insufficient knowledge of the detailed rupture processes, effects due to small scale 3D heterogeneity may not be simulated just with stochastic source processes. For example, Love waves only appear on the tangential component, and Rayleigh waves will not appear on tangential components for a 1D layered model. To account for 3D scattering, we introduce a mechanism to transfer energy from one component to the other as follows:

$$\begin{pmatrix} u_z(\omega) \\ u_R(\omega) \\ u_T(\omega) \end{pmatrix} = \left[1/J(\omega) \begin{pmatrix} 1 + S_{ZZ}(\omega) & S_{ZR}(\omega) & S_{ZT}(\omega) \\ S_{RZ}(\omega) & 1 + S_{RR}(\omega) & S_{RT}(\omega) \\ S_{TZ}(\omega) & S_{TR}(\omega) & 1 + S_{TT}(\omega) \end{pmatrix} \right]^{\left(\frac{d}{l(\omega)}\right)} \begin{pmatrix} U_z(\omega) \\ U_R(\omega) \\ U_T(\omega) \end{pmatrix}$$

where *Sxy* is the scattering coefficient that scatters energy from the *y*th component to the *x*th component for single scattering, *l(ω)* is the free path length, and the power of

d/l is meant to simulate multiple scattering for longer propagation length. The free path length $l(\omega)$ is shorter for high frequency (Sato and Fehler, 2000), arguing for more scattering at short wavelength. u is the ground motion after scattering and U is the ground motion for 1D structures, and $J(\omega)$ is the Jacobian which ensures that total energy is conserved after scattering. We assume that the scattering coefficients $Sxy(\omega)$ has two parts, the amplitude strength part and the phase strength part, and is assumed to take the form of

$$Sxy(\omega) = \epsilon_{xy} e^{i\psi}$$

where ψ is a dimensionless parameter indicating phase shifts due to scattering, and ε is the amplitude strength of scattering, which depends on the components involved and the heterogeneity level of the 3D structure. To account for larger scattering between R and T, and less scattering between R and Z, or R and Z, we choose $\varepsilon_{RZ}=\varepsilon_{ZR}=\varepsilon_{ZT}=\varepsilon_{TZ}=0.5$, and assume $\varepsilon_{ZZ=ZTT}=\varepsilon_{RR=}\ \varepsilon_{RT}=\varepsilon_{TR}$. It is assumed that $\varepsilon_{RR}=5\%$ of energy is scattered with phase shift of $\psi= 0.1\ \pi$ with single scattering. Frequency dependent free path length $l(\omega)$ is approximated with the power law $l(\omega)=l_0\omega^n$, where we choose n=1 for simplicity. l_0 is chosen in such a way that the 1 Hz waveform is still deterministic (2-3 fold scattering) at a distance of 80 km (twice the crustal thickness), while the waveform becomes more stochastic at 3Hz (5-10 fold scattering), and becomes completely stochastic beyond 3Hz.

3.3. Some examples of ground motion simulation with the above algorithm

We modified the frequency-wave number code (FK) (Zhu and Rivera, 2002) with the above algorithms. Since the FK code works in the frequency - wave number domain, our deterministic-stochastic algorithm is naturally implemented in the frequency domain. Because of the loss of precision problem associated with the Haskell propagation matrix at high frequencies (Aki and Richards, 2002), we only compute ground motion up to 10 Hz with the modified FK algorithms. We introduce a frequency dependence in the radiation pattern (Pitarka et al., 2000). At frequencies of 1 Hz and less, we use the theoretical radiation pattern. Between 1 and 3 Hz, we linearly interpolate between the theoretical radiation pattern and the average radiation coefficients of Boore and Boatwright (1984), causing coherence of the radiation pattern to decrease with increasing frequency. Above 3 Hz, we use a constant average radiation coefficient. Ground motion simulation of higher frequencies (up to 50 Hz) is computed with ray theory as presented in the following sections.

For event Mt Carmel, we compute synthetic seismograms at station USIN with a deterministic radiation pattern (frequency independent) and a frequency dependent radiation pattern (Figure 16). Station USIN lies close to a node of the Mt Carmel earthquake, so the tangential component is much stronger than the radial and vertical component for both sets of synthetic seismograms at low frequency. But at high frequency (>2Hz), the radial and vertical components become stronger for the case of frequency dependent radiation pattern, similar to what is observed in the recorded data.

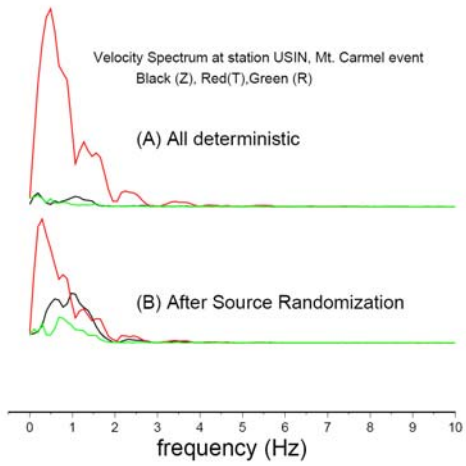

Figure 16. Spectrum of synthetic seismograms with deterministic radiation pattern (top) and with frequency dependent radiation pattern (bottom).

4. Q of the Central and Eastern US

Q is an important parameter for high frequency ground motion simulations. Numerous previous studies have demonstrated large Q differences between western US and CEUS. Mitchell (1981) reported that in the upper crust (top 20km), Q is 275, 165 and 80 for CEUS, Colorado Plateau and Basin and Range respectively. For the lower crust, the Q difference is small and Q is about 1000. Boore (2003) presents a summary of Q for different regions of the world, and also emphasizes the large differences in Q between the western US and CEUS. Atkinson (2004) assumes a frequency dependent $Q = 893\ f^{0.32}$ for eastern North America (ENA), which translate into Q>1000 for high frequencies (> 2Hz).

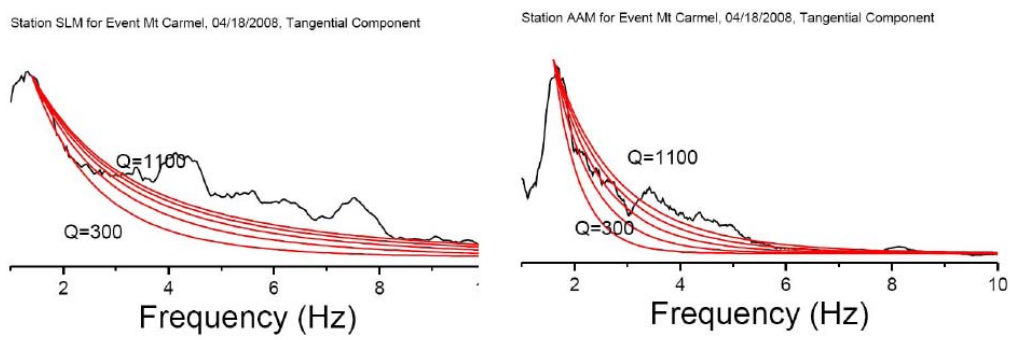

Figure 17. Effects of Q on the spectrum for station SLM (left) and AAM (right). The lowest red curve is for Q=300, and Q increases by 200 for each higher red curve.

We also verify the ENA Q model with the broadband seismograms recorded from the Mt Carmel earthquake. In Figure 17, we compare synthetic spectra (red) and observed spectra for station SLM and AAM. The synthetic spectra are computed with the following equation:

$$u(f) = S(f)\exp(-\pi fT/Q)$$

where T is the travel time of the S wave and can be calculated with the 1D layered model for given distance and focal depth, *S(f)* is the source spectrum of Mt Carmel event, and *u(f)* is the spectrum of the synthetic ground motion. From Figure 17, we observe that a Q of 900-1100 can produce reasonable fit, consistent with Atkinson (2004)'s model. For simplicity, we adopt a Q model of Q(f)=900 $f^{0.32}$ for CEUS.

5. High frequency (>1Hz) ground motion simulation in Central and Eastern US

The high frequency simulation methodology sums the response for each subfault assuming a random phase, an omega-squared source spectrum and simplified Green's functions. The methodology follows from Boore (1983) with the extension to finite-faults given by Frankel (1995) and Hartzell et al (1999). Each subfault is allowed to rupture with a subfault moment weighting that is proportional to the final static slip amount given by the prescribed rupture model. The final summed moment is then scaled to the prescribed target mainshock moment. The convolution operator of Frankel (1995) scales the subevent rise time to the target rise time. Additionally, this operator also ensures that the result is not dependent on the choice of the subfault dimensions.

Beresnev and Atkinson (1997) define a radiation-strength factor (s), which is used as a free parameter in the specification of the subfault corner frequency (f_c)

$$f_c = s \cdot z \frac{V_r}{\pi \cdot dl} \qquad (3)$$

where z is a scaling factor relating f_c to the rise time of the subfault source, V_r is the rupture velocity and dl is the subfault dimension. In our approach, instead of allowing this to be a free parameter, we set $z=C$ (constant) and let

$$s = \begin{cases} 1 & \text{if } h < h_0 \\ 1 + c_0 \dfrac{h - h_0}{h_1 - h_0} & \text{if } h_0 \le h \le h_1 \\ 1 + c_0 & \text{if } h \ge h_1 \end{cases} \qquad (4)$$

where $h_0 = 5\,\text{km}$, $h_1 = 10\,\text{km}$ and h is the depth of the subfault center in km. Based on calibration experiments, c_0 is set at 0.4. Since the corner frequency is proportional to slip velocity (inversely proportional to rise time), this formulation replicates the observed trend that slip velocity is relatively low for shallow ruptures and increases with increasing rupture depth (Kagawa et al., 2004), causing the ground motions from surface faulting earthquakes to be weaker than those of earthquakes that do not break the ground surface (Somerville, 2003; Somerville and Pitarka, 2006). These observations are now reflected in most of the newly developed NGA ground motion models for tectonically active regions (Power et al., 2008) through a new source parameter, the depth to top of rupture, which we proposed. For active tectonic regions, we set z=1.6. In CEUS, we find rise time is about 1.85 times longer than for active regions, which suggests z=0.9 for CEUS applications.

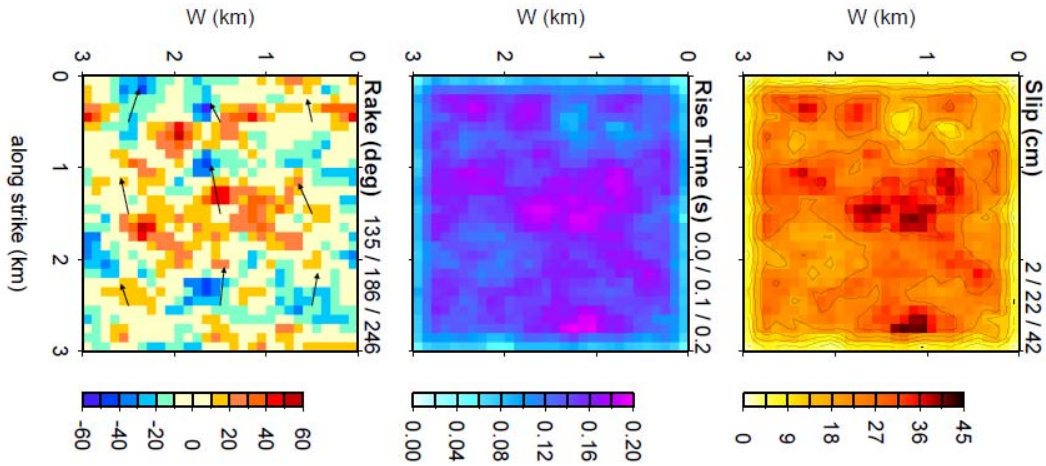

Figure 18. A finite fault model of rake angle (left), rise time (middle) and slip for the Mt Carmel event.

We note that although this formulation reduces the number of free parameters, it certainly is not unique and probably has trade-offs with other parameters in the stochastic model. In particular, allowing the subfault stress parameter (σ_p) to be variable across the fault would accommodate a similar type of slip velocity scaling. For active tectonic regions, we fix $\sigma_p = 50$ in our simulations. For CEUS applications, the stress parameter is typically a factor of 2-3 times larger than found for active tectonic regions (e.g., Atkinson and Boore, 2006). This change in stress parameter most likely reflects the difference in rupture area for CEUS events relative to active regions, which is a factor of 2.5. Scaling the stress parameter by this factor yields a value of $\sigma_p = 125$ for CEUS applications.

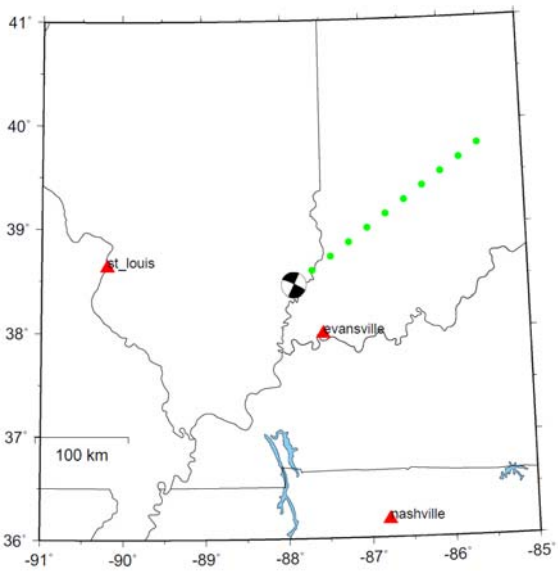

Figure 19. Location of sites (green dots) for ground motion simulation. The beach ball represents the Mt Carmel earthquake.

Our formulation allows the specification of a plane layered velocity model from which we calculate simplified Green's functions (GFs) and impedance effects. The GFs are comprised of the direct and Moho-reflected rays, which are attenuated by $1/R_p$ where R_p is the path length traveled by the particular ray. For each ray, we calculate a radiation pattern coefficient by averaging over a range of slip mechanisms and take-off angles. Anelasticity is incorporated using a travel-time weighted average of the Q values for each of the velocity layers and using a generic rock-site kappa operator. Finally, gross impedance effects are included using quarter wavelength theory (Boore and Joyner, 1997) to derive amplification functions that are consistent with the specified velocity structure.

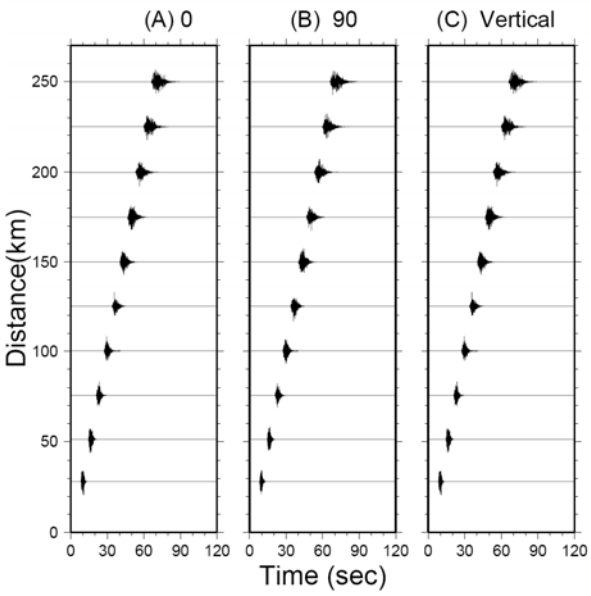

Figure 20. High frequency ground acceleration computed without the Moho-reflected ray. The amplitude of each waveform is normalized.

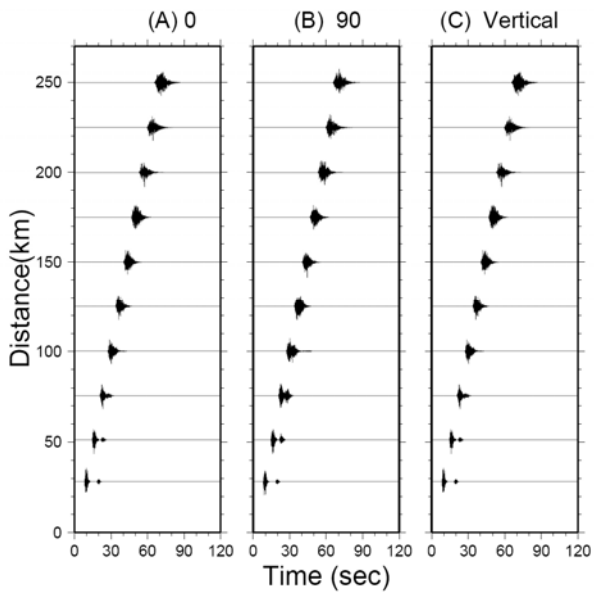

Figure 21. High frequency ground acceleration computed with the Moho-reflected ray SmS. The amplitude of each waveform is normalized.

We generate a finite fault model for the Mt Carmel earthquake (Figure 19) with randomized rake angle, rise time and slip (Figure 18), whose distribution follows a k^2 law in the wave number domain. We also keep the total moment of all the sub-faults the same as that determined in Section 1. In Figures 20 and 21, we display synthetic ground acceleration without and with the Moho-reflected ray (SmS) respectively. Inclusion of SmS makes ground motion last longer, as well as become stronger for post-critical distances. When six Moho reflection multiples are taken into account, the synthetic wave trains (Figure 22) look much more like the observed high frequency ground motion (Figure 23), suggesting that multiple Moho reflections need to be taken into account.

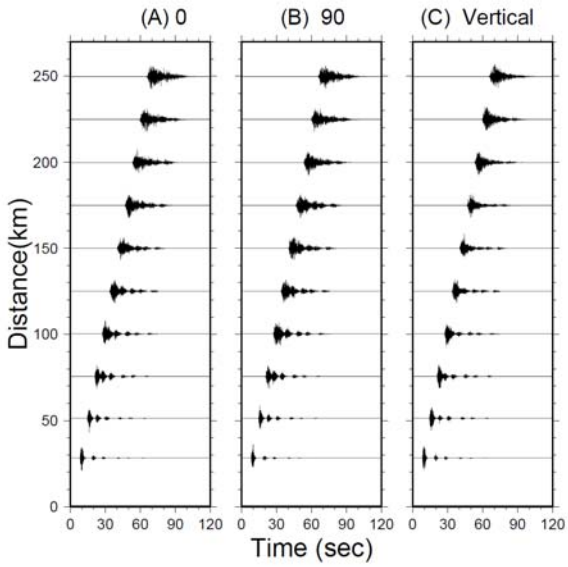

Figure 22. High frequency ground acceleration computed with six Moho-reflection multiples The amplitude of each waveform is normalized.

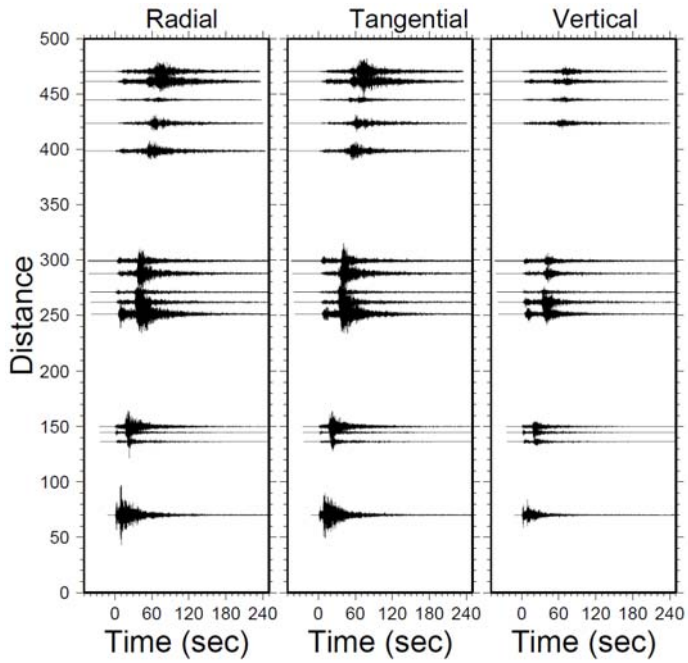

Figure 23. Observed record section of high frequency (high pass filter > 2Hz) ground

acceleration for Mt Carmel earthquake. The ground motion shows little attenuation.

We also test the effect of Q on high frequency ground motion simulations. In Figure 24, we display simulated ground motion for Qo=300 and Qo=900 respectively. Geometrical spreading factors have been removed for easier comparison of amplitudes at different distances. Obviously Qo=300 predicts ground motion that are too small at large distances (300-500km), but the ground motion with Qo=900 matches the general features of the observations (Figure 23) fairly well. This indicates that Qo=900 is a good approximation of the Q model in CEUS.

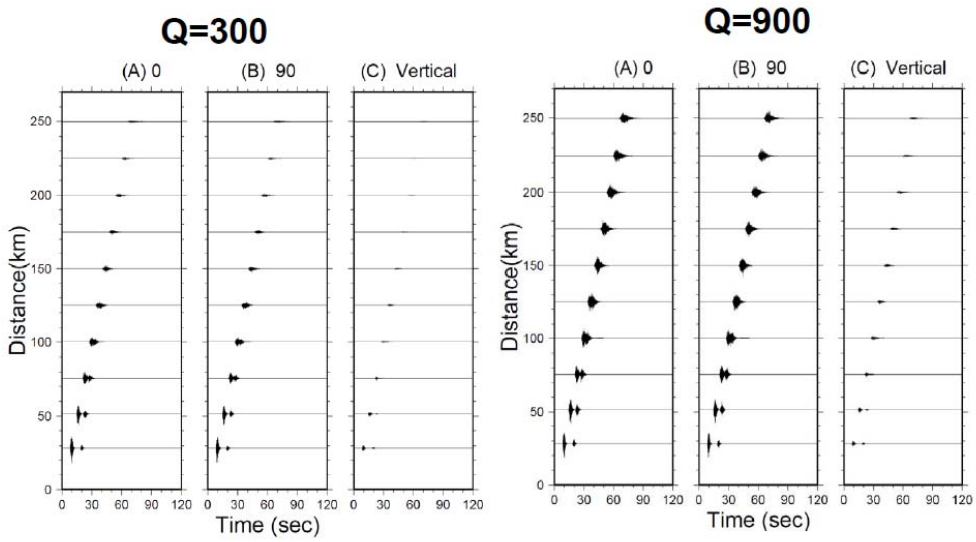

Figure 24. High frequency ground motion simulation for Q=300 (left three panels) and Q=900 (right three panels). Amplitude has been corrected for geometrical spreading.

We only include crustal S waves in the high frequency ground simulations, assuming that P waves and mantle S waves (Sn) have negligible strength. This is probably appropriate for the western US where ground motions only have significant amplitudes at frequencies lower than 10Hz. Groud motions at frequencies higher than 10 Hz in the western US are not a concern because of the lower Q. However, for the CEUS, the extremely high Q makes high frequency (>10Hz) ground motions much larger. In Figure 25, we display ground motions in different frequency bands, and it is observed that P wave amplitudes are comparable to those of S, and Sn is also not negligible for frequencies above 12.5 Hz. This observation suggests that future high frequency ground motion studies should take P waves and Sn waves into account.

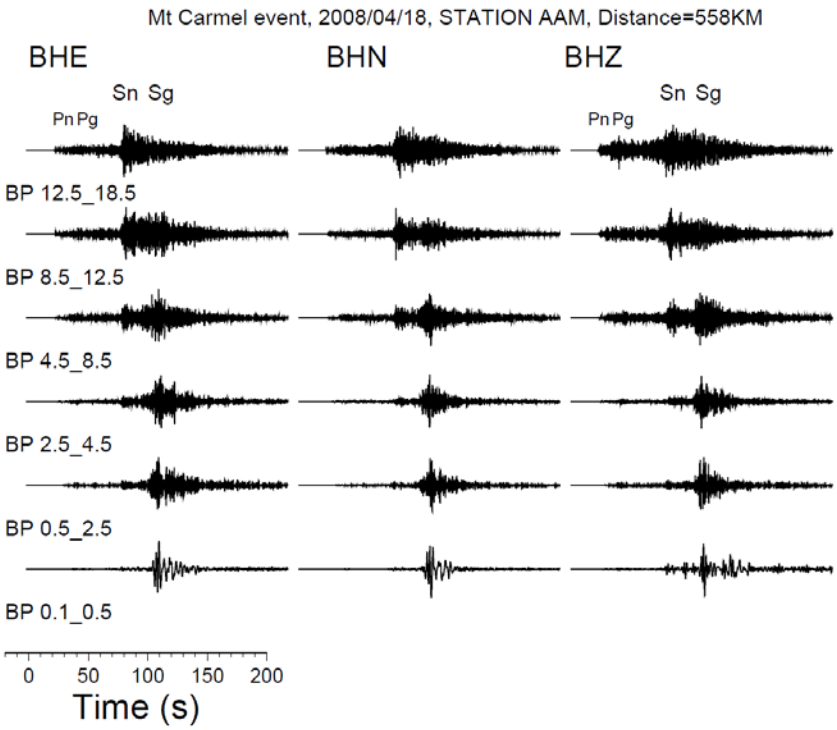

Figure 25. Bandpass filtered (with frequency band marked to the left) three component velocity seismic records (BHE,BHN, BHZ) at station AAM from the Mt. Carmel event. For frequency > 4.5 Hz , the P wave is not negligible compared to S, and Sn, the mantle wave is stronger than Sg/Lg, the crustal waves.

References

Abrahamson, N.A., P.G. Somerville, and C. Allin Cornell (1990). Uncertainty in numerical strong motion predictions, *Proc. 4th U.S. National Conference on Earthquake Engineering,* **1**, 407-416.

Atkinson, G.M. (2004). Empirical Attenuation of Ground-Motion Spectral Amplitudes in Southeastern Canada and the Northeastern United States, *Bull. Seism. Soc. Am*. **94**, 1079-1095.

Atkinson, G.M. and D.M. Boore (2006). Earthquake Ground-Motion Prediction Equations for Eastern North America, *Bull. Seism. Soc. Am*. **96**, 2181-2205.

Atkinson, G. (1993). Source spectra for earthquakes in eastern North America. *Bull. Seism. Soc. Am.* 83, 1778-1798.

Atkinson, G. and D. Boore (1995). New ground motion relations for eastern North America, *Bull. Seism. Soc. Am.* 85, 17-30.

Atkinson, G.M. and P.G. Somerville (1994). Calibration of time history simulation methods, *Bull. Seism. Soc. Am*., **84**, 400-414.

Beresnev I. and G. Atkinson (1997). Modeling finite fault radiation from the ωn spectrum, *BSSA*. **87**, 67-84.

Boatwright, J. and G. Choy (1992). Acceleration source spectra anticipated for large

earthquakes in eastern North America, *Bull. Seism. Soc. Am.,* 82, 660-682.

Boore, D. M. (1983). Stochastic simulation of high-frequency ground motions based on seismological models of the radiated spectra. *Bull. Seism. Soc. Am.*, **73**, 1865–1894.

Boore, D. M. and W. B. Joyner (1997). Site amplifications for generic rock sites. *Bull. Seism. Soc. Am*., **87**, 327–341.

Burger, R.W., P.G. Somerville, J.S. Barker, R.B. Herrmann, and D.V. Helmberger (1987). The effect of crustal structure on strong ground motion attenuation relations in eastern North America, *Bull. Seism. Soc. Am*., **77**, 420-439.

Campbell, K.W. and Bozorgnia, Y., 2008, NGA ground motion model for the geometric mean horizontal component of PGA, PGV, PGD, and 5%-damped linear elastic response spectra for periods ranging from 0.01 to 10 s, *Earthquake Spectra*, **24**, 139-171.

Chiou, B. S. J. and R. R. Youngs (2006). Chiou and Youngs PEER-NGA empirical ground motion model for the average horizontal component of peak acceleration and pseudo-spectral acceleration for spectral periods of 0.01 to 10 seconds, *Pacific Earthquake Engineering Research Center*, University of California, Berkeley, CA.

Chung, W-Y., A.C. Johnston, and J. Pujol (1992). A global study of stable continental interplate earthquakes: focal mechanisms, source-scaling relations, and seismotectonics. EPRI RP-2556-54, Electric Power Research Institute, Palo Alto, California, 252 pp.

Day, S., 1982, Three dimensional simulation of spontaneous rupture: The effect of non-uniform pre-stress, *Bull. Seism. Soc. Am*., **72**, 1881-1902.

Du, W.-X., W.-Y. Kim and L.R. Sykes (2003). Earthquake Source Parameters and State of Stress for the Northeastern United States and Southeastern Canada from Analysis for Regional Seismograms, *Bull. Seism. Soc. Am*. **93**, 1633-1648.

Ebel, J.E., P.G. Somerville, and J.D. McIver (1986). A study of source parameters of some large earthquakes in northeastern North America, *J. Geophys. Res*., **91**, 8231-8247.

Electric Power Research Institute (1993). Guidelines for determining design basis ground motions. Volume 1. Method and guidelines for estimating earthquake ground motion in eastern North America. Report EPRI TR-102293.

Electric Power Research Institute (1994). The earthquakes of stable continental regions. Report EPRI TR-102261-V1.

Frankel, A. (1995). Simulating strong motions of large earthquakes using recordings of small earthquakes: the Loma Prieta mainshock as a test case. *Bull. Seism. Soc. Am*., **85**, 1144–1160.

Frankel, A. (2009). A constant stress-drop model for producing broadband synthetic seismograms: Comparison with the Next Generation Attenuation relations, *Bull. Seism. Soc. Am*., 99, 664-680.

Graves, R.W., P. Somerville, N. Collins, A. Pitarka and S. Ni (2007). Analysis of strong ground motions from the June 12, 2005 Anza earthquake. Report to CSMIP Data Interpretation Project, California Geological Survey.

Graves, R. W. and A. Pitarka (2004). Broadband time history simulation using a hybrid approach, *Proc. 13th World Conference on Earthquake Engineering*, Vancouver,

Canada. paper no. 1098.
Hartzell, S., S. Harmsen, A. Frankel, and S. Larsen (1999). Calculation of broadband time histories of ground motion: Comparison of methods and validation using strong-ground motion from the 1994 Northridge earthquake, *Bull. Seism. Soc. Am.*, **89**, 1484–1504.
Hartzell, S., C. Langer and C. Mendoza (1994). Rupture histories of eastern North American earthquakes. *Bull. Seism. Soc. Am.* 84, 1703-1724.
Helmberger, D. V. (1983). Theory and application of synthetic seismograms. In Earthquakes: *Observation, Theory and Interpretation*, ed. H. Kanamori, 174–222. Bologna, Italy: Società Italiana di Fisica. In English.
Herrmann, R. B., M. Withers, and H. Benz, The April 18, 2008 Illinois earthquake : An ANSS monitoring success, Seismol. Res. Lett., 79, 830{843, 2008.
Ichinose, G., P. Somerville, H.K. Thio, S. Matsushima and T. Sato (2005). Rupture process of the 1948 Fukui earthquake (M 7.1) from the joint inversion of seismic waveform and geodetic data. J. Geophys. Res. 110, B05301, doi:10.1029/2004JB003437.
Irikura, K. (1983). Semi-empirical estimation of strong ground motions during large earthquakes, *Bull. Disaster Prevention Res. Inst. (Kyoto Univ).* 33, 63-104.
Ji, C. and G. Hayes, (2008). Preliminary result of the May 12, 2008 Mw 7.8 Eastern Sichuan, China earthquake. http://earthquake.usgs.gov/eqcenter/eqinthenews/2008/us2008ryan/finite_fault.php
Johnston, A.C. (1996). Seismic moment assessment of earthquakes in stable continental regions III. New Madrid 1811-1812, Charleston 1886 and Lisbon 1755, Geophys. J. Int. 126, 314-344.
Joyner, W.B. and D.M. Boore (1986). On simulating large earthquakes by Green's function addition of smaller earthquakes, in: Proceedings of the 5th Maurice Ewing Symposium on Earthquake Source Mechanics, American Geophysical Union, p. 269-274.
Kagawa, T., K. Irikura, and P. G. Somerville (2004). Differences in ground motion and fault rupture process between the surface and buried rupture earthquakes, *Earth, Planets, and Space*, **56**, 3–14.
Kwok, A.O. and Stewart, J.P., 2006, Application of theoretical 1D amplification factors for evaluation of seismic site effects, *Bull. Seism. Soc. Am.*, **96**, 1422-1436.
Kim, W.-Y. (2003). 18 June 2002 Caborn, Indiana Earthquake: reactivation of Ancient Rift in the Wabash Valley Seismic Zone? *Bull. Seism. Soc. Am.* 93, 2201–2211.
Kim, W.-Y. (1998). The ML Scale in Eastern North America, *Bull. Seism. Soc. Am.* 88, 935-951.
Komatitsch, D., and Tromp, J., 1999. Introduction to the spectral-element method for 3-D seismic wave propagation*, Geophys. J. Int.,* 139, 806-822.
Langston, C.A. (1987). Depth of faulting during the 1968 Meckering, Australia earthquake sequence determined from waveform analysis of local seismograms, *J. Geophys. Res., 87,* 11561-11574.
Liu P., R. J. Archuleta and S. H. Hartzell, 2006, Prediction of Broadband Ground-Motion Time Histories: Hybrid Low/High- Frequency Method with

Correlated Random Source Parameters, *Bull. Seism. Soc. Am*. 96, 2118–2130.

Ma, S. and G.M. Atkinson (2006). Focal Depths for Small to Moderate Earthquakes ($m_N \geq 2.8$) in Western Quebec, Southern Ontario, and Northern New York, *Bull. Seism. Soc. Am*. **96**, 609-623.

Mai, P. and G. Beroza (2002). A spatial random field model to characterize complexity in earthquake slip, *J. Geophys. Res*., **107**(B11), doi:10.1029/2001JB000588.

Miao, Q and C.A. Langston (2007). Empirical Distance Attenuation and the Local-Magnitude Scale for the Central United States, *Bull. Seism. Soc. Am*. **97**, 2137-2151.

Mitchell B, 1981, Regional variation and frequency dependence of Qß in the crust of the United States, *Bull. Seism. Soc. Am*. 71, 1531-1538

Marone, C. and C.H. Scholz (1988). The depth of seismic faulting and the upper transition from stable to unstable slip regimes, *Geophys. Res. Lett*. 15, 621-624.

OU, G.-B. and HERRMANN, R. B. (1990), A Statistical Model for Ground Motion Produced by Earthquakes at Local and Regional Distances, *Bull. Seismol. Soc. Am.* 80, 1397–1417.

Petersen, M., A. Frankel, A., S. Harmsen, C. Mueller, K. Haller, R. Wheeler, R. Wesson, Y. Zeng, O. Boyd, D. Perkins, N. Luco, E. Field, C. Wills, and K. Rukstales (2008). Documentation for the 2008 updated of the United States National Seismic Hazard Maps. *U.S. Geological Survey Open File Report* 2008-1128.

Saikia, C. K. (1994). Modified frequency-wave-number algorithm for regional seismograms using Filon's quadrature–modeling of L(g) waves in eastern North America, *Geophys. J. Int.* 118, 142–158.

Pitarka, A., P.G. Somerville, Y. Fukushima, T. Uetake, and K. Irikura (2000). Simulation of near-fault ground motion using hybrid Green's functions. *BSSA*. 90, 556-586.

Power, M., B. Chiou, N. Abrahamson, Y. Bozorgnia, T. Shantz, and C. Roblee (2008). An overview of the NGA Project. Earthquake Spectra, in press.

Reasenberg, P., and W.L. Ellsworth (1982). Aftershocks of the Coyote Lake, California, earthquake of August 6, 1979: a detailed study, *J. Geophys. Res., 87,* 10637-10655.

Ritsema, J. and T. Lay (1995). Long period regional wave moment tensor inversion for earthquakes in the western United States. J. Geophys. Res. 100, 9853-9864.

Saikia, C.K. and P.G. Somerville (1997). Simulated hard-rock motions in Saint Louis, Missouri, from large New Madrid earthquakes (Mw > 6.5). Bull. Seism. Soc. Am. 87, 123-139.

Saikia, C.K., P.G. Somerville, H.K. Thio, N.F. Smith, A. Pitarka, B.B. Woods (1998). Crustal structure and ground motion models in the eastern and Central United States from National Seismograph Network Data. NUREG/CR-6593, U.S. Nuclear Regulatory Commission.

Saikia, C.K., P.G. Somerville, D.V. Helmberger, M.K. Sen, J.P. McLaren, L.J. Burdick, and N.F. Smith (1989). Ground-Motion Attenuation and Earthquake Source Scaling in Eastern North America, Electric Power Research Institute, 307 pp.

Saikia, C.K., P.G. Somerville, H.K. Thio, N.F. Smith, A. Pitarka, B.B. Woods (1998). Crustal structure and ground motion models in the eastern and Central United States

from National Seismograph Network Data. NUREG/CR-6593, U.S. Nuclear Regulatory Commission.

Savy, J. (1997). Ground motion attenuation in eastern North America. Section 4.3 of Report on Trial SHAC Methodology Implementation Project, Lawrence Livermore National Laboratory.

Seeber, L., W. Y. Kim, J. Armbruster, W. Du, and A. Lerner-Lam (2002). The 20 April 2002 *M*w 5.0 earthquake near Au Sable Forks, Adirondacks, New York: a first glance at a new sequence, *Seism. Res. Lett.* **74,** 480–489.

Sibson, R.H. (1984). Roughness at the base of the seismogenic zone: contributing factors, *J. Geophys. Res., 89*, 5791-5799.

Somerville, P.G., R. Graves, S. Ni, S. Song, and N. Collins (2008). Earthquake source and strong ground motion models for Australia. Draft Report to Geoscience Australia.

Somerville, P.G. and A. Pitarka (2006). Differences in earthquake source and ground motion characteristics between surface and buried earthquakes. *Proceedings of the Eighth National Conference on Earthquake Engineering,* San Francisco, California.

Somerville, P.G. (2003). Magnitude scaling of the near fault rupture directivity pulse. *Phys. Earth. Planetary. Int*., 137, 201-212.

Somerville, P.G., N. Collins, N. Abrahamson, R. Graves and C. Saikia (2001). Earthquake source scaling and ground motion attenuation relations for the central and eastern United States. Report to the U.S. Geological Survey, Grant No. 99H.QGR0098

Somerville, P.G., K. Irikura, R. Graves, S. Sawada, D. Wald, N. Abrahamson, Y. Iwasaki, T. Kagawa, N. Smith and A. Kowada (1999). Characterizing earthquake slip models for the prediction of strong ground motion. *Seismological Research Letters* 70, 59-80.

Somerville, P., C.K. Saikia, D. Wald, and R. Graves (1996). Implications of the Northridge earthquake for strong ground motions from thrust faults, *Bull. Seism. Soc. Am.,* 86, S115- S125.

Somerville, P.G., N.F. Smith, and R.W. Graves (1994). The effect of critical Moho reflections on the attenuation of strong motion from the 1989 Loma Prieta earthquake, in *"The Loma Prieta, California, Earthquake of October 17, 1989 - Strong Ground Motion,"* U.S. Geological Survey Professional Paper 1551-A, A67-A75.

Somerville, P.G., J.P. McLaren, C.K. Saikia, and D.V. Helmberger (1990). The November 25, 1988 Saguenay, Quebec earthquake: source parameters and the attenuation of strong ground motion. *Bull. Seism. Soc. Am.,* **80**, 1118-1143.

Somerville, P.G., J.P. McLaren, L.V. LeFevre, R.W. Burger and D.V. Helmberger (1987). Comparison of source scaling relations of eastern and western North American earthquakes, *Bull. Seism. Soc. Am*., **77**, 332-346.

SSHAC (1996). Probabilistic seismic hazard analysis: a consensus. Senior Seismic Hazard Analysis Committee, USDOE, USNRC, EPRI.

Toro, G.R., N.A. Abrahamson, and J.F. Schneider (1997). Modeling of strong ground motions from earthquakes in Central and Eastern North America: best estimates and uncertainties. *Seism. Res. Lett*. 68, 41-57.

Walling, M., Silva, W.J., and Abrahamson, N.A., 2008, Non-linear site amplification

factors for constraining the NGA models, *Earthquake Spectra*, **24**, accepted for publication.

Wheeler, R.L. and A. Frankel (2000). Geology in the 1996 USGS seismic hazard maps, central and eastern United States. *Seismological Research Letters* 71, 273-282.

Zeng Y. and J. A. Anderson (1995), A method for direct computation of the differential seismogram with respect to the velocity change in a layered elastic solid, *Bull. Seism. Soc. Am.* 85, 300-307.

Zhu, L. and D. Helmberger (1996). Advancement in source estimation techniques using broadband regional seismograms, *Bull. Seism. Soc. Am.*, **86**, 1634-1641.

Zhu L. and L.A. Rivera, 2002, A note on the dynamic and static displacements from a point source in multilayered media, *Geophysical Journal Int.*, 148, 619–627